light results in absorption) (*23*) is 8 W/m^2, composed of smoke negative forcing of –28 W/m^2 and cloud reduction positive forcing of +22 W/m^2. The sensitivity of the forcing to the value of SSA is linear. For SSA = 0.88, the forcing increases to 13 W/m^2; for SSA = 0.94, the forcing decreases to 3 W/m^2.

The 24-hour average forcing is estimated on the basis of observations (Fig. 1) that the lifetime of the boundary layer cloud fields is 4 ± 2 afternoon hours, shorter than the duration of the smoke (10 ± 2 hours). Therefore, the 24-hour average of combined clouds and smoke forcing is –5.5 ± 2 W/m^2, instead of forcing of smoke only of –11.5 ± 2 W/m^2. Inclusion of the smoke semi-direct effect reduces to less than half the 24-hour average forcing from previous estimates (*24*, *25*) and converts the instantaneous forcing in the afternoon to positive forcing (warming) rather than negative forcing (cooling) for the smoke alone.

The proposed mechanism for the smoke reduction of cloud fraction can be described as a combination of a few dependent feedback processes. The first is the direct aerosol effect on stabilizing the boundary layer by heating of the aerosol layer and cooling of the surface caused by the aerosol scattering and absorption (shading the surface from solar flux). This process by itself reduces the convectivity and boundary layer cloud formation. Second, reduction of solar flux reaching the canopy tends to decrease evapotranspiration and the moisture input to the atmosphere (*26*). The small amount of moisture released by evapotranspiration in smoky conditions remains near the canopy because of decreased turbulent fluxes within the boundary layer. Third, because of the heating of the aerosol layer by absorption, the capacity of the layer to hold water vapor increases and there is less likelihood to reach supersaturation and form clouds. The fourth process is the competition for water vapor by the extremely high concentrations of particles that share the condensed water and keep the layer from reaching supersaturation (*27*, *28*). Detailed descriptions of the aerosol effects and feedbacks are given in (*29*).

Analysis of satellite data has documented the relationship between heavy aerosol and the formation of scattered cumulus clouds. Possible effects on deeper convection have so far been ignored. Even though the smoke aerosol in the Amazon absorbs light one-tenth as much as it scatters light, the absorption is enough to heat the atmosphere by 2° to 4°C per day and to change the energy balance between the surface and the atmosphere in a way that stabilizes the boundary layer. However, for a neutral atmosphere, stabilizing one layer of the atmosphere destabilizes the layer above it. If the humidity can penetrate the inversion at the top of the smoke layer, then it will reach a very unstable layer, creating larger deep convective clouds (*30*). Such clouds can be observed sporadically in the satellite images, but with no correlation to the presence of the smoke. Our results show that smoke, instead of cooling the climate, warms it in the afternoon hours when the scattered cumulus clouds can form. The 24-hour forcing reduces the net forcing to –5.5 ± 2 W/m^2, less than half of net forcing from smoke alone. The reduction in cloud fraction by absorbing aerosol may be an important mechanism to explain why Earth warmed substantially in the last century despite the expected aerosol cooling effect.

References and Notes

1. Intergovernmental Panel on Climate Change, *Climate Change 2001—The Scientific Basis* (*Contribution of Working Group I to the Third Assessment Report of the Intergovernmental Panel on Climate Change*) (Cambridge Univ. Press, Cambridge, 2001).
2. S. Twomey, *J. Atmos. Sci.* **34**, 1149 (1977).
3. A. B. Albrecht, *Science* **245**, 1227 (1989).
4. D. Rosenfeld, *Science* **287**, 1793 (2000).
5. V. Ramanathan, P. J. Crutzen, J. T. Kiehl, D. Rosenfeld, *Science* **294**, 2119 (2001).
6. Y. J. Kaufman, D. Tanré, O. Boucher, *Nature* **419**, 215 (2002).
7. S. K. Satheesh, V. Ramanathan, *Nature* **405**, 60 (2000).
8. T. Eck, B. N. Holben, I. Slutsker, A. Setzer, *J. Geophys. Res.* **103**, 31865 (1998).
9. J. Hansen, M. Sato, R. Ruedy, *J. Geophys. Res.* **102**, 6831 (1997).
10. A. S. Ackerman *et al.*, *Science* **288**, 1042 (2000).
11. A. J. Heymsfield, G. M. McFarquhar, *J. Geophys. Res.* **106**, 28653 (2001).
12. J. Lelieveld *et al.*, *Science* **298**, 794 (2002).
13. P. Alpert *et al.*, *Geophys. Res. Lett.* **29** (11), 10.1029/2001GL013554 (2002).
14. S. Menon, J. Hansen, L. Nazarenko, Y. Luo, *Science* **297**, 2250 (2002).
15. E. Salati, in *The Forest and the Hydrological Cycle: Geophysiology of Amazonia*, R. E. Dickinson, Ed. (Wiley, New York, 1987), pp. 273–296.
16. C. A. Nobre, L. F. Mattos, C. P. Dereczynski, T. A. Tarasova, I. V. Trosnikov, *J. Geophys. Res.* **103**, 31809 (1988).
17. See supporting data on *Science* Online.
18. E. Kalnay *et al.*, *Bull. Am. Meteorol. Soc.* **77**, 437 (1996).
19. J. V. Martins *et al.*, *Geophys. Res. Lett.* **29** (12), 10.1029/2001GL013252 (2002).
20. Y. J. Kaufman *et al.*, *J. Geophys. Res.* **102**, 17051 (1997).
21. M.-D. Chou, *J. Atmos. Sci.* **49**, 762 (1992).
22. M.-D. Chou, D. P. Kratz, W. Ridgway, *J. Clim.* **4**, 424 (1991).
23. O. Dubovik *et al.*, *J. Atmos. Sci.* **59**, 590 (2002).
24. J. E. Penner, R. E. Dickinson, C. A. O'Neill, *Science* **256**, 1432 (1992).
25. P. V. Hobbs, J. S. Reid, R. A. Kotchenruther, R. J. Ferek, R. Weiss, *Science* **275**, 1776 (1997).
26. D. Cohan, J. Xu, M. H. Bergin, W. L. Chameides, *Global Biogeochem. Cycles* **16** (4), 10.1029/2001GB001441 (2002).
27. H. Yu, S. C. Liu, R. E. Dickinson, *J. Geophys. Res.* **107** (D12), 10.1029/2001JD000754 (2002).
28. G. Feingold, L. A. Remer, J. Ramaprasad, Y. J. Kaufman, *J. Geophys. Res.* **106**, 22907 (2002).
29. M. Z. Jacobson, *J. Geophys. Res.* **107** (D19), 10.1029/2001JD001376 (2002).
30. Y. Rudich, A. Sagi, D. Rosenfeld, *J. Geophys. Res.* **108**, 4478 (2003).

31. This research was performed while I.K. held a National Research Council Research Associateship Award at NASA/GSFC.

Supporting Online Material

www.sciencemag.org/cgi/content/full/303/5662/1342/DC1
SOM Text
Figs. S1 to S5
References

21 July 2003; accepted 5 January 2004

Laser Guide Star Adaptive Optics Imaging Polarimetry of Herbig Ae/Be Stars

Marshall D. Perrin,[1,2]* James R. Graham,[1,2] Paul Kalas,[1,2] James P. Lloyd,[2,3] Claire E. Max,[2,4] Donald T. Gavel,[2,5] Deanna M. Pennington,[2,4] Elinor L. Gates[2,6]

We have used laser guide star adaptive optics and a near-infrared dual-channel imaging polarimeter to observe light scattered in the circumstellar environment of Herbig Ae/Be stars on scales of 100 to 300 astronomical units. We revealed a strongly polarized, biconical nebula 10 arc seconds (6000 astronomical units) in diameter around the star LkHα 198 and also observed a polarized jet-like feature associated with the deeply embedded source LkHα 198-IR. The star LkHα 233 presents a narrow, unpolarized dark lane consistent with an optically thick circumstellar disk blocking our direct view of the star. These data show that the lower-mass T Tauri and intermediate mass Herbig Ae/Be stars share a common evolutionary sequence.

Diffraction-limited optical and infrared astronomy from the ground requires adaptive optics (AO) compensation to eliminate atmospheric wavefront disturbances. Bright stars may be used as wavefront references for this correction, but most astronomical targets lack nearby guide stars. AO observations of these targets from the ground can only be accomplished with the use of artificial laser guide stars (LGS) (*1*).

Herbig Ae/Be stars are young stars with masses between 1.5 and 10 times that of the sun; they are the intermediate-mass counter-

parts of the more common T Tauri stars. Excess infrared and millimeter emission shows that Herbig Ae/Be stars are associated with abundant circumstellar dust (*2*). Visible and near-infrared (NIR) light scattered from dust is typically polarized perpendicular to the scattering plane (*3*), making polarimetry a useful tool for probing the distribution of this material (*4*). Although Herbig Ae/Be stars are intrinsically very luminous, many are so distant or extincted that they are too faint to act as their own wavefront references and thus require LGS AO.

The Herbig Ae/Be stars LkHα 198 and LkHα 233 (table S1) were observed on 22 July 2003 at the 3-m Shane telescope at Lick Observatory (fig. S1) with the use of the Lawrence Livermore National Laboratory LGS AO system (*5*) and the Berkeley NIR camera IRCAL (*6*). The atmospheric seeing was 0.8 arc sec at 550 nm, and the AO-corrected wavefront produced images with Strehl ratios of about 0.05 to 0.1 at 2.1 μm and full width at half maximum resolution of 0.27 arc sec (*7*).

IRCAL's imaging polarimetry mode uses a cryogenic $LiYF_4$ Wollaston prism to produce two simultaneous images of orthogonal polarizations. The sum of the two channels gives total intensity, and the difference gives a Stokes polarization. The dominant noise source near bright stars in AO images is an uncorrected seeing halo. Because this halo is unpolarized and thus vanishes in the difference image, dual-channel polarimetry enhances the dynamic range in circumstellar environments (*8*). We have adopted the observing and data reduction techniques (*9*).

LkHα 198 is located at the head of an elliptical loop of optical nebulosity extending 40 arc sec to the star's southeast (*10*). This complex region 600 pc distant includes a molecular CO outflow (*11*) and two Herbig-Haro jets (*12*), as well as two additional Herbig Ae/Be stars in the immediate vicinity (V376 Cas and LkHα 198-IR) (*13*) and a millimeter source (LkHα 198-MM) believed to be a deeply embedded protostar (*14*). This proximity of sources requires high resolution observations to disentangle the relationships between the various components (*15*). We identified a biconical nebula ~10 arc sec in diameter [6000 astronomical units (AU)], oriented north-south, with polarization vectors concentric with respect to LkHα 198 (Fig. 1). The lobes of the reflection nebula are divided by a dark, unpolarized lane that we interpret as a density gradient toward the equatorial plane of a circumstellar disk and/or a flattened envelope. The north-south orientation indicates that LkHα 198 is unlikely to have created the giant elliptical nebula or the molecular outflow to the southeast. However, it is consistent with LkHα 198 being the source for the Herbig-Haro flow at a position angle (PA, measured east from north) of 160°, a conclusion supported by the extension of the polarized reflection nebula along this PA. However, this is 20° away from the observed symmetry axis of the nebula, requiring an inner disk axis tilted or precessing with respect to the outer envelope.

The embedded source LkHα 198-IR (*16*) is detected in our *H* and K_s band data 5.5 arc sec from LkHα 198 at PA = 5°. A polarized, extremely blue, jet-like feature extends >2 arc sec (1200 AU) from LkHα 198-IR at PA = 105° (*17*). The polarization vectors of this apparent jet are perpendicular to its long axis, indicating that LkHα 198-IR is the illuminating source, not LkHα 198. The jet appears to be half of a parabolic feature opening toward the southeast, with its apex at LkHα 198-IR and its southern side partially obscured by the envelope around LkHα 198. We suggest that the northwest side of a bipolar structure around LkHα 198-IR may be hidden at NIR wavelengths by the dust indicated by millimeter observations (*18*). The orientations of circumstellar structures revealed by our images confirm that LkHα 198-IR is the best candidate for the origin of the Herbig-Haro outflow to PA 135°, though on the basis of geometrical considerations we cannot entirely exclude the protostar LkHα 198-MM. By extension, the large elliptical nebula was most likely created by outflow from LkHα 198-IR, although we see it primarily in scattered light from the optically much brighter LkHα 198.

LkHα 233 is an embedded A5e-A7e Herbig Ae/Be star that is associated with a blue, rectangular reflection nebula 50 arc sec in extent, located in the Lac OB1 molecular cloud at 880 pc. Our imaging polarimetry reveals four distinct lobes bisected by a narrow, unpolarized lane with PA ≈ 150° (Fig. 1). The nebulosity around LkHα 233 is extremely blue in the NIR, with its east-west extent decreasing from 6 arc sec (5300 AU) at *J* and *H* to 2 arc sec (1800 AU) at K_s. The orientation of the lobes relative to the dark lane suggests that they are the limb-brightened edges of a conical cavity in a dusty envelope illuminated by a highly extincted star. The radial extent of the dark lane (1000 AU) suggests that it is associated with an equatorial torus characteristic of a flattened infalling protostellar cloud (*19*) and not a rotationally supported disk.

We find that the intensity peak of the star is shifted southwest relative to the polarization centroid, with the displacement increasing from 0.15 arc sec at K_s to 0.35 arc sec at *J*. This too indicates that the lane consists of optically thick foreground material that has a flattened spatial distribution consistent with a circumstellar disk or infalling protostellar cloud. We do not see the star directly but instead view a scattering surface above the disk midplane.

Our results are consistent with lowresolution, wide-field optical imaging polarimetry (*20*), which suggests a circumstellar torus in the northwest-southeast direction perpendicular to a bipolar reflection nebula. Our interpretation is also consistent with the existence of an optical [S II] emission line jet (*21*) blue-shifted to the southwest. The jet both bisects the nebulosity and lies perpendicular to the proposed disk. The geometry of the reflection nebula indicates that the outflow is only poorly collimated ($\Delta\theta \approx 70°$) despite the apparently narrow jet traced by optical forbidden line emission. Because [S II] line emission arises preferentially in regions denser than the critical density for this transition, the surface brightness distributions can take on the appearance of a highly collimated jet, despite the fact that the streamlines collimate logarithmically slowly (*22*).

Observations of T Tauri stars have led to a general understanding of the origin of solar-type stars (*23*): The fragmentation and collapse of an interstellar cloud creates a self-gravitating protostar surrounded by a Keplerian accretion disk fed by an infalling, rotationally flattened envelope. The disk mediates the outflows common to low-mass young stellar objects, which play a key role in the dispersal of the natal gas and dust.

It has been hypothesized that the more massive Herbig Ae/Be stars and the T Tauri stars form and evolve in similar manners (*24*), but this remains controversial. On large spatial scales, the disk-like nature of the circumstellar matter around Herbig Ae/Be stars is well established. Flattened structures around several sources have been resolved on 100-AU scales (*25*) or have Keplerian kinematics (*26*). However, the evidence seems to be ambiguous on scales of tens of AU and below, with some authors arguing for a spherical geometry (*27*) and others favoring disks (*28*).

LkHα 198 and LkHα 233 are both classified as Hillenbrand group II Herbig Ae/Be stars: They have infrared spectra that are flat or rising toward longer wavelengths. This means that they are young stars that may or may not possess circumstellar disks but do possess circumstellar envelopes that are not confined to a disk plane. We observe such envelopes around both of our sources in the form of centrosymmetrically polarized biconical nebulosities viewed about edge-on to the midplanes.

We compared our observations with radiative transfer models computed for a sequence of circumstellar dust distributions around T Tauri stars (*29*, *30*). These models provide both total

[1]Astronomy Department, University of California Berkeley, Berkeley, CA 94720, USA. [2]National Science Foundation Center for Adaptive Optics, University of California Santa Cruz, 1156 High Street, Santa Cruz, CA 95064, USA. [3]Astronomy Department, California Institute of Technology, 1201 East California Boulevard, Pasadena, CA 91125, USA. [4]Lawrence Livermore National Laboratory, 7000 East Avenue, Livermore, CA 94550, USA. [5]Laboratory for Adaptive Optics, University of California Santa Cruz, 1156 High Street, Santa Cruz, CA 95064, USA. [6]University of California Observatories/Lick Observatory, Post Office Box 85, Mount Hamilton, CA 95140, USA.

*To whom correspondence should be addressed. E-mail: mperrin@astro.berkeley.edu

and polarized intensity images, which we convolved with a model instrumental point-spread function to match our observed resolution (fig. S2). Bipolar outflow cavities in these models produce a limb-brightened appearance at near-infrared wavelengths, with the brightening stronger in polarized light than in total intensity.

For both LkHα 233 and LkHα 198, the peak polarization differs between the two lobes. These asymmetries may indicate the sign of the inclination of each object. In Whitney's model envelopes, which use dust grain properties fit to an extinction curve for the Taurus molecular cloud, the closer lobe was brighter overall but had lower fractional polarization by several percent. For LkHα 198, the polarization in the northern lobe of the bipolar nebulosity is generally 10 to 15% lower than that of the southern lobe at all wavelengths (20% compared with 35% at *H*, for instance), suggesting that the northern lobe is oriented toward us. For LkHα 233, the southwest lobe is 14% polarized on average compared with 26% for the northeast lobe. This result indicates that the southern lobe is facing us, consistent with the blueshift of the CO jet in that direction and the southwest shift of the intensity peak relative to the polarization centroid.

LkHα 233's limb-brightened appearance provides compelling evidence for the presence of cavities swept out by bipolar outflow from the star. Cavity models with an opening angle of 30° to 40° seen at an inclination of 80° reproduce both the observed polarization fraction of 25 to 40% and the higher degree of limb brightening seen in the near lobe.

The absence of limb brightening may be evidence that LkHα 198 lacks polar cavities or at most possesses very narrow ones. The detectability of limb brightening for a given angular resolution depends on the opening angle between the symmetry axis and edge of the cavity. At our resolution, envelope models with cavity opening angles greater than ~20° predict detectable limb brightening, whereas we observed for

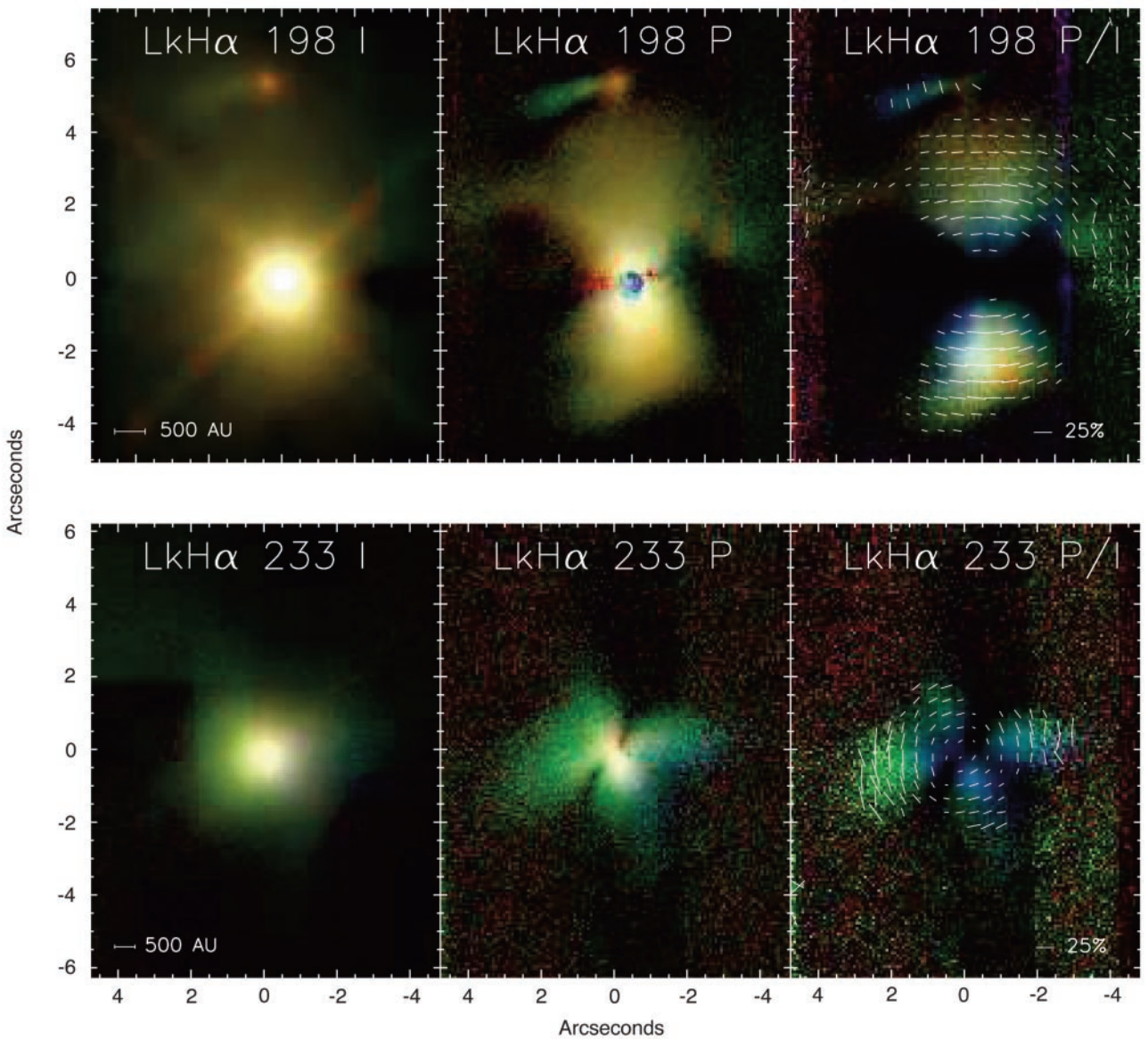

Fig. 1. Three-color LGS AO mosaics of LkHα 198 (**top**) and LkHα 233 (**bottom**). Plotted from left to right for each object are the total intensity (Stokes *I*), the polarized intensity $\{P = \sqrt{[(Q^2 + U^2)]}\}$, and the polarization fraction (*P*/*I*). *I* and *P* are displayed with the use of log stretches, whereas *P*/*I* is shown on a linear stretch. Red is K_s band (2.1 μm); green, *H* (1.6 μm); and blue, *J* (1.2 μm). Polarization vectors for *H* band are overplotted on the *P*/*I* image; although the degree of polarization changes somewhat between bands, the position angles do not vary much. Integration times per band were 960 and 1440 s for LkHα 198 and LkHα 233, respectively. The dimmest circumstellar features detected in our polarimetric observations are about 1×10^4 to 2×10^4 fainter than the stellar intensity peaks. The IRCAL polarimeter is sensitive to polarization fractions as low as a few percent, resulting in a signal-to-noise ratio of 5 to 10 per pixel for the typical polarizations of 15 to 40% observed around our targets.

LkHα 198 an opening angle of 45° without limb brightening. Thus, our observations do not support the presence of evacuated cavities in the envelope of LkHα 198. The observed morphology can instead be explained by the illumination of a cavity-free, rotationally flattened envelope by the central star; the bipolar appearance would then arise from light escaping along the path of least optical depth. However, these cavity-free infalling envelope models have opening angles that increase with wavelength, whereas we observe a constant opening angle, suggesting a geometric rather than optical depth origin for the observed morphology. This discrepancy may be resolvable by varying the dust particle properties.

On the basis of these observations, LkHα 233 is the more evolved of the two systems, with well-defined cavities swept out by bipolar outflow and bisected by a very dark lane. LkHα 198 is a less evolved system, which is only in the early stages of developing bipolar cavities and possesses lower extinction in the apparent disk midplane.

The observed circumstellar environments are consistent with the rotationally flattened infall envelopes models developed for T Tauri stars, indicating that the process of envelope collapse has similar phases, despite the large disparities in mass and luminosity between these two classes of young stars. This morphological similarity leads us to infer that the conservation and transport of angular momentum is the dominant physical process for both classes of stars. Alternate formation pathways have been suggested for OB stars that invoke new physical mechanisms, such as magnetohydrodynamic turbulence (*31*) or stellar mergers (*32*). The Herbig Ae stars studied here appear to be below the mass threshhold at which such effects become important.

References and Notes

1. W. Happer, G. J. MacDonald, C. E. Max, F. J. Dyson, *J. Opt. Soc. Am.* **11**, 263 (1994).
2. L. A. Hillenbrand, S. E. Strom, F. J. Vrba, J. Keene, *Astrophys. J.* **397**, 613 (1992).
3. P. Bastien, *Astrophys. J.* **317**, 231 (1987).
4. D. A. Weintraub, A. A. Goodman, R. L. Akeson, in *Protostars and Planets IV*, V. Mannings, A. P. Boss, S. S. Russell, Eds. (Univ. of Arizona Press, Tucson, AZ, 2000), pp. 247–271.
5. C. Max *et al.*, *Science* **277**, 1649 (1997).
6. J. P. Lloyd *et al.*, *Proc. SPIE* **4008**, 814 (2000).
7. Additional information on materials and methods is available as supporting material on *Science* Online.
8. D. E. Potter *et al.*, *Astrophys. J.* **540**, 422 (2000).
9. J. R. Kuhn, D. Potter, B. Parise, *Astrophys. J.* **553**, L189 (2001).
10. W. Li, N. J. Evans, P. M. Harvey, C. Colome, *Astrophys. J.* **433**, 199 (1994).
11. J. Canto, L. F. Rodriguez, N. Calvet, R. M. Levreault, *Astrophys. J.* **282**, 631 (1984).
12. D. Corcoran, T. P. Ray, P. Bastien, *Astron. Astrophys.* **293**, 550 (1995).
13. R. Hajjar, P. Bastien, *Astrophys. J.* **531**, 494 (2000).
14. G. Sandell, D. A. Weintraub, *Astron. Astrophys.* **292**, L1 (1994).
15. C. D. Koresko, P. M. Harvey, J. C. Christou, R. Q. Fugate, W. Li, *Astrophys. J.* **485**, 213 (1997).
16. P. O. Lagage *et al.*, *Astrophys. J. Lett.* **417**, L79+ (1993).
17. M. Fukagawa *et al.*, *J. Psychiatry Neurosci.* **54**, 969 (2002).
18. T. Henning, A. Burkert, R. Launhardt, C. Leinert, B. Stecklum, *Astron. Astrophys.* **336**, 565 (1998).
19. S. Terebey, F. H. Shu, P. Cassen, *Astrophys. J.* **286**, 529 (1984).
20. C. Aspin, M. J. McCaughrean, I. S. McLean, *Astron. Astrophys.* **144**, 220 (1985).
21. M. Corcoran, T. P. Ray, *Astron. Astrophys.* **336**, 535 (1998).
22. F. Shu *et al.*, *Astrophys. J.* **429**, 781 (1994).
23. F. H. Shu, F. C. Adams, S. Lizano, *Annu. Rev. Astron. Astrophys.* **25**, 23 (1987).
24. F. Palla, S. W. Stahler, *Astron. J.* **418**, 414 (1993).
25. V. Mannings, A. I. Sargent, *Astrophys. J.* **490**, 792 (1997).
26. V. Mannings, D. W. Koerner, A. I. Sargent, *Nature* **388**, 555 (1997).
27. J. di Francesco, N. J. Evans, P. M. Harvey, L. G. Mundy, H. M. Butner, *Astrophys. J.* **432**, 710 (1994).
28. A. Natta *et al.*, *Astron. Astrophys.* **371**, 186 (2001).
29. B. A. Whitney, K. Wood, J. E. Bjorkman, M. J. Wolff, *Astrophys. J.* **591**, 1049 (2003).
30. B. A. Whitney, K. Wood, J. E. Bjorkman, M. Cohen, *Astrophys. J.* **598**, 1079 (2003).
31. C. F. McKee, J. C. Tan, *Astrophys. J.* **585**, 850 (2003).
32. I. A. Bonnell, M. R. Bate, H. Zinnecker, *Mon. Not. R. Astron. Soc.* **298**, 93 (1998).

33. We thank the Lick Observatory staff who assisted in these observations, including T. Misch, K. Chloros, and J. Morey; the many individuals who have contributed to making the laser guide star system a reality; and B. Whitney for providing us with electronic versions of models. Onyx Optics fabricated our YLF Wollaston prisms. Supported in part by NSF Science and Technology Center for Adaptive Optics, managed by the University of California at Santa Cruz under cooperative agreement AST-9876783 and also under the auspices of the U.S. Department of Energy, National Nuclear Security Administration, by the University of California, Lawrence Livermore National Laboratory, under contract W-7405-Eng-48. P.K. received additional support from the NASA Origins Program (grant NAG5-11769). M.D.P. is supported by a NASA Michelson Graduate Fellowship, under contract to the Jet Propulsion Laboratory (JPL). JPL is managed for NASA by the California Institute of Technology.

Supporting Online Material

www.sciencemag.org/cgi/content/full/303/5662/1345/DC1
Materials and Methods
Figs. S1 and S2
Table S1

11 December 2003; accepted 23 January 2004

Single-Crystal Nanorings Formed by Epitaxial Self-Coiling of Polar Nanobelts

Xiang Yang Kong, Yong Ding, Rusen Yang, Zhong Lin Wang*

Freestanding single-crystal complete nanorings of zinc oxide were formed via a spontaneous self-coiling process during the growth of polar nanobelts. The nanoring appeared to be initiated by circular folding of a nanobelt, caused by long-range electrostatic interaction. Coaxial and uniradial loop-by-loop winding of the nanobelt formed a complete ring. Short-range chemical bonding among the loops resulted in a single-crystal structure. The self-coiling is likely to be driven by minimizing the energy contributed by polar charges, surface area, and elastic deformation. Zinc oxide nanorings formed by self-coiling of nanobelts may be useful for investigating polar surface–induced growth processes, fundamental physics phenomena, and nanoscale devices.

Self-assembly of nanocrystals can be driven by van der Waals forces and hydrogen bonding among the passivating organic molecules on the particle surfaces (*1–3*). For inorganic nanostructures that expose charge-polarized surfaces, such as nanobelts of oxides like ZnO (*4*), electrostatic forces can drive self-assembly, especially in gas-phase environments where these forces are unscreened by solvents. For crystalline nanomaterials grown in a solid-vapor environment, one type of polar charge–induced helical and spiral ZnO structure was previously reported (*5*). We now report a distinct nanoring structure that is formed by spontaneous self-coiling of a polar nanobelt during growth. Nanoring growth appears to be initiated by circular folding of a nanobelt driven by long-range electrostatic interactions. Short-range chemical bonding among the loops leads to the final single-crystalline structure. The self-coiling is driven by minimizing the energy contributed by polar charges, surface area, and elastic deformation.

Single-crystal nanorings of ZnO were grown by a solid-vapor process. The raw material was a mixture of ZnO (melting point 1975°C), indium oxide, and lithium carbonate powders at a weight ratio of 20:1:1, and it was placed at the highest temperature zone of a horizontal tube furnace. Before heating to a desired temperature of 1400°C, the tube furnace was evacuated to $\sim 10^{-3}$ torr to remove the residual oxygen. The source materials were then heated to 1400°C at a heating rate of 20°C/min. ZnO decomposes into Zn^{2+} and O^{2-} at high temperature (1400°C) and low pressure ($\sim 10^{-3}$ torr), and this decomposition process is the key step for controlling the anisotropic growth of the nanobelts. After a few

School of Materials Science and Engineering, Georgia Institute of Technology, Atlanta, GA 30332–0245 USA.

*To whom correspondence should be addressed. E-mail: zhong.wang@mse.gatech.edu